

How the diffusivity profile reduces the arbitrariness of protein folding free energies

M. Hinczewski,^{1,2} Y. von Hansen,¹ J. Dzubiella,¹ and R. R. Netz^{1,a)}

¹*Department of Physics, Technical University of Munich, 85748 Garching, Germany*

²*Institute for Physical Science and Technology, University of Maryland, College Park, Maryland 20742, USA*

(Received 26 January 2010; accepted 11 May 2010; published online 28 June 2010)

The concept of a protein diffusing in its free-energy folding landscape has been fruitful for both theory and experiment. Yet the choice of the reaction coordinate (RC) introduces an undesirable degree of arbitrariness into the problem. We analyze extensive simulation data of an α -helix in explicit water solvent as it stochastically folds and unfolds. The free-energy profiles for different RCs exhibit significant variations, some having an activation barrier, while others not. We show that this variation has little effect on the predicted folding kinetics if the diffusivity profiles are properly taken into account. This kinetic quasi-universality is rationalized by an RC rescaling, which, due to the reparameterization invariance of the Fokker–Planck equation, allows the combination of free-energy and diffusivity effects into a single function, the rescaled free-energy profile. This rescaled free energy indeed shows less variation among different RCs than the bare free energy and diffusivity profiles separately do, if we properly distinguish between RCs that contain knowledge of the native state and those that are purely geometric in nature. Our method for extracting diffusivity profiles is easily applied to experimental single molecule time series data and might help to reconcile conflicts that arise when comparing results from different experimental probes for the same protein. © 2010 American Institute of Physics. [doi:10.1063/1.3442716]

I. INTRODUCTION

The problem of protein folding kinetics is formidable from a purely statistical mechanics point of view: The unfolded protein, in other words the entire ensemble of microstates that significantly deviate from the native state, transits via a myriad of distinct pathways to the folded (native) state, and trying to predict folding times from basic principles is obviously hopeless. Yet, robust features have emerged both from experiments and theoretical concepts.^{1,2} A key fact is that any experiment that probes protein folding or unfolding projects protein microstates onto a low-dimensional (typically one-dimensional) observable. For example, circular dichroism in the far ultraviolet and infrared adsorption spectroscopy basically measure the average helicity, while fluorescence is sensitive to side chain contacts or local solvent structure around tryptophan residues.^{3,4} Kinetic information at ambient conditions and on short time scales relevant for fast folding events can be obtained by time-resolved spectroscopy after flash photoheating⁵ or by fluorescence resonance/triplet-triplet energy transfer (FRET/TTET) correlation studies that couple to the distance between a donor and acceptor linked to two positions along the peptide chain.^{6,7} More recently, single-molecule spectroscopic techniques have allowed the observation of time-dependent folding/unfolding of individual proteins, thus going beyond ensemble averaging.^{8,9} Likewise, single molecule studies where forces are applied at two points along the peptide

backbone probe the distance between those two anchoring points.¹⁰ All these experimental observables in fact constitute distinct *reaction coordinates* (RCs).

Exponential distributions of folding times found for many (but not all) proteins using different techniques suggest two-state-folding as a quite general paradigm of folding kinetics: here the folded and unfolded states are separated by a free-energy barrier along the respective RC.⁴ Even proteins folding via many intermediate states can produce a single-exponential folding time distribution if there exists a rate-limiting transition. Therefore, as long as the RC of choice distinguishes the two states connected by the rate-limiting step, using different kinds of measurement/RC would likely generate similar single-exponential kinetics even in such a case. Similar conclusions can be drawn from the direct observation of population distributions, where a free-energy barrier means that folding intermediates are rarely observed.^{8,9} The recent observation that different experimental techniques yield different kinetics¹¹ or distribution functions^{12,13} when applied to the same protein casts doubt on the clear division between two-state (exhibiting a free-energy barrier) and downhill folders (without such a barrier). In this paper we argue that such inconsistencies can arise when implicitly referring to different RCs, and show a way how to reconcile conflicting results.

In theoretical studies, various RCs have become popular to characterize the folding transition, either because they approximately correspond to an experimentally accessible observable or because they are simple to calculate. The radius of gyration, the fraction of native contacts between residues,

^{a)}Author to whom correspondence should be addressed. Electronic mail: netz@ph.tum.de.

or the mean distance from the native state are typical examples.^{14,15} More complex topological order parameters such as the contact order have been suggested for describing universal features of protein folding kinetics.¹⁶ In the theoretical framework that naturally emerges, the protein diffuses along the RC, governed by a stochastic equation and subject to deterministic forces encrypted in the free-energy landscape, as well as stochastic forces due to the random environment.^{17–19} Early on, it was realized that the diffusion constant in this coarse-grained picture is an effective quantity that takes into account the connectivity between states (i.e., the number of possible connecting paths), the energetic ruggedness of such paths,²⁰ as well as orthogonal degrees of freedom.²¹ As folding progresses, internal friction starts to play a more dominating role,^{22,23} while solvent friction becomes less important as more and more peptide groups lose solvent contact.⁵ Recently, the simplification of a constant diffusivity was abandoned and a diffusivity profile was extracted from simulations of peptides: these works either considered proteins without solvent (and thus exclude variations of the solvent friction)^{24–26} or considered exclusively short-time dynamics and thus are not applicable to global folding kinetics.²⁷ The trifold coupling between the choice of a specific RC and the free energy and diffusivity profiles in the presence of explicit solvent has remained elusive.

In this paper, we perform an in-depth analysis of long MD trajectories of an α -helix-forming oligopeptide including explicit water. Such model peptides form the subject of detailed experimental studies and constitute some of the simplest peptides that exhibit nontrivial folding kinetics.²⁸ They are thus interesting in their own right and at the same time—due to their minute size—allow for realistic modeling over times much longer than their folding times, including solvent degrees of freedom.²⁹ As a prerequisite for our analysis, we introduce a simple way of extracting diffusivity profiles from time series data for an arbitrary RC, which can be conveniently applied to experimental spectroscopic data,⁹ or force spectroscopic data for RNA,³⁰ or proteins³¹ as well. We demonstrate that different RCs for one and the same protein trajectory are associated with substantially different free-energy profiles, some showing a barrier separating the folded and unfolded helix state, some showing no barrier at all (which is not surprising and has been found in different contexts before³²). This resembles the experimental findings in connection with the dispute on downhill versus two-state folding,^{12,13} but is resolved by accounting for the spatially inhomogeneous diffusivity: The diffusivity profiles are full of structure and show considerable variation among different RCs. No simple connection between the free energy and diffusivity profiles seems to exist. Yet, the folding kinetics predicted using a stochastic approach based on the free-energy landscape is largely independent of the RC if and only if the diffusivity profile is taken into account. Thus, the variance between free-energy profiles along different RCs gives rise to kinetic universality if the coupling to diffusivity is included (where we distinguish between RCs that contain knowledge of the native state and those that are purely geometric in nature). This specifically means that the presence of a free-energy barrier (i.e., absence of intermediate states) is

in principle compatible with both exponential and nonexponential kinetics, and that different experimental probes are bound to measure different free-energy profiles. The same conclusions also apply to more refined or optimized RCs.^{33–37} Full understanding of protein folding kinetics thus requires measuring both average distributions and kinetic trajectories. Similar conclusions were very recently drawn from a Bayesian analysis of folding trajectories of simple coarse-grained model peptides based on implicit-solvent simulations.²⁶ Since α -helices are a prominent folding motif, the features we find are most likely relevant for more complex proteins as well.

II. METHODS

A. Simulations

Standard all-atom molecular dynamics (MD) simulations provide 1.1 μ s trajectories of an alanine (A)-based peptide with sequence Ace-AEAAAKEEAAKA-Nme in explicit water,²⁹ which is a shortened version of similar sequences with charged Glu⁺(E) and Lys⁻(K) residues at positions i and $i+4$ that experimentally are known to spontaneously form α -helices.²⁸ The mechanism for α -helix formation involves, in addition to the stabilizing influence of E-K salt bridges, hydration effects.^{29,38} The MD simulations utilize the parallel module sander.MPI in the AMBER 9.0 package with the ff03 force-field and the TIP3P water model at a pressure of 1 bar and a temperature T fixed by a Berendsen barostat and Langevin thermostat, respectively.³⁹ The periodically repeated cubic simulation box has an edge length $L \approx 36$ Å including ≈ 1500 water molecules. Electrostatic interactions are calculated by particle mesh Ewald summation and real-space electrostatic and van der Waals interactions are cut off at 9 Å. As a check on the convergence of the standard MD simulation, replica-exchange MD (REMD) simulations are performed with the AMBER10 simulation package.³⁹ Here, the same force-field and system parameters as in the other standard MD simulations are employed, apart from switching to a constant volume ensemble. 32 replicas are considered in a temperature range between 265 and 520 K, with each replica simulated for 22.5 ns, amounting to a total sampling time of 720 ns. Temperature exchanges between neighboring replicas are attempted every 250 integration steps, leading to an exchange rate of 10%–30%.

B. Reaction coordinates

Trajectory analysis is performed using the *ptraj* tool in the AMBER package.³⁹ The helicity (i.e., the α -helical fraction) is identified using the DSSP method by Kabsch and Sander.⁴⁰ In addition, we focus on five different RCs to follow the folding kinetics (Table I):

- (i) Q_1 , defined as the root-mean-square distance from a fully helical reference structure, averaged over all M atoms of the peptide. The reference structure was chosen randomly from configurations which display 100% helicity, with little variation depending on the specific choice.

TABLE I. List of RCs used in the paper.

RC notation	Description
Q_1	RMS deviation from perfect helix
Q_2	Native intrabackbone hydrogen bond length
Q_3	Inverse native hydrogen bond length
Q_4	Radius of gyration
Q_5	End-to-end distance

- (ii) The mean native hydrogen bond (HB) length, $Q_2 = \sum_{i=1}^{N-4} r_{i,i+4} / (N-4)$, averaged over all $N=14$ residues including the acetyl (Ace) and amine (Nme) end caps, where $r_{i,j}$ is the distance between HB forming atoms, i and j , in the peptide backbone.
- (iii) The mean inverse HB length, $Q_3 = 1 - (N-4)^{-1} \sum_{i=1}^{N-4} r_{i,i+4}^0 / r_{i,i+4}$, where $r_{i,i+4}^0 \approx 2 \text{ \AA}$ is the native HB length in the folded state, defined by the most probable length of each $(i, i+4)$ HB.
- (iv) The radius of gyration, $Q_4 = [\sum_{i,j=1}^M r_{i,j}^2 / (2M^2)]^{1/2}$, a measure for the average peptide size and accessible in scattering.
- (v) Q_5 , the distance between the centers of mass of the end caps.

Trajectories are recorded with a resolution of 20 ps, giving a total of 54171 data points. To compare different RCs with each other, we exclude for each RC the 11 smallest and 11 largest values, and define rescaled RCs

$$q_i = (Q_i - Q_i^{\min}) / (Q_i^{\max} - Q_i^{\min}), \quad (1)$$

such that the minimal and maximal values of the remaining 54 149 data points, denoted as Q_i^{\min} and Q_i^{\max} , are projected on the RC values $q_i=0$ and $q_i=1$, respectively.

C. Diffusion constant

We assume that the stochastic time evolution of a given RC is described by the one-dimensional Fokker–Planck (FP) equation⁴¹

$$\frac{\partial}{\partial t} \Psi(Q, t) = \frac{\partial}{\partial Q} D(Q) e^{-\beta F(Q)} \frac{\partial}{\partial Q} \Psi(Q, t) e^{\beta F(Q)}, \quad (2)$$

where $\Psi(Q, t)$ is the probability of having a configuration with RC value Q at time t , $D(Q)$ is the (in general Q -dependent) diffusivity, $\beta = 1 / (k_B T)$ and $\beta F(Q) = -\ln \langle \Psi(Q) \rangle$ is the free energy, where $\langle \Psi(Q) \rangle$ is the time-averaged probability distribution. A few methods to extract $D(Q)$ from time series data based on Bayesian analysis of transition rates^{34,42} or short-time fluctuations have been described.^{25,27} Our method extracts $D(Q)$ directly from folding times. Define $\tau_{\text{FP}}(Q, Q^f)$ as the mean first passage (MFP) time to go from a state Q to some final state Q^f without recrossing Q^f , corresponding to an adsorbing boundary condition at Q^f . For the case $Q > Q^f$ one finds⁴³

$$\tau_{\text{FP}}(Q, Q^f) = \int_{Q^f}^Q dQ' \frac{e^{\beta F(Q')}}{D(Q')} \int_{Q'}^{Q^{\max}} dQ'' e^{-\beta F(Q'')}, \quad (3)$$

and for $Q < Q^f$ one has

$$\tau_{\text{FP}}(Q, Q^f) = \int_Q^{Q^f} dQ' \frac{e^{\beta F(Q')}}{D(Q')} \int_{Q^{\min}}^{Q'} dQ'' e^{-\beta F(Q'')}, \quad (4)$$

where at Q^{\min} and Q^{\max} reflective (zero-flux) boundary conditions hold. By differentiation with respect to Q , we obtain the diffusivity for $Q > Q^f$

$$D(Q) = \frac{e^{\beta F(Q)}}{\partial \tau_{\text{FP}}(Q, Q^f) / \partial Q} \int_Q^{Q^{\max}} dQ' e^{-\beta F(Q')}, \quad (5)$$

and for $Q < Q^f$ as

$$D(Q) = - \frac{e^{\beta F(Q)}}{\partial \tau_{\text{FP}}(Q, Q^f) / \partial Q} \int_{Q^{\min}}^Q dQ' e^{-\beta F(Q')}. \quad (6)$$

An even simpler procedure employs the *round-trip time*

$$\tau_{\text{RT}}(Q, Q^f) = \text{sign}(Q - Q^f) [\tau_{\text{FP}}(Q, Q^f) + \tau_{\text{FP}}(Q^f, Q)], \quad (7)$$

the magnitude of which is the time needed to start at Q , reach Q^f for the first time, start from Q^f again and reach back to Q for the first time. One finds

$$\tau_{\text{RT}}(Q, Q^f) = Z \int_{Q^f}^Q dQ' \frac{e^{\beta F(Q')}}{D(Q')}, \quad (8)$$

where $Z = \int_{Q^{\min}}^{Q^{\max}} dQ e^{-\beta F(Q)}$ is the partition function. The diffusivity profile based on the round-trip time reads

$$D(Q) = \frac{Z e^{\beta F(Q)}}{\partial \tau_{\text{RT}}(Q, Q^f) / \partial Q}. \quad (9)$$

Intuitively, the slope of the round-trip time function is inversely proportional to $D(Q)$. For a given $F(Q)$, a larger slope implies a slower return to the starting point, or equivalently a smaller local diffusivity. The FP approach assumes an underlying Markovian process, meaning that $D(Q)$ and thus $\partial \tau_{\text{RT}}(Q, Q^f) / \partial Q$ are independent of Q^f . We exploit (and check) this by defining a mean round-trip time function $\bar{\tau}_{\text{RT}}(Q)$ that results from an average of round-trip times $\tau_{\text{RT}}(Q, Q^f)$ over their final states Q^f . Since on the FP level $\tau_{\text{RT}}(Q, Q^f)$ curves for different Q^f differ only by an additive constant, we should be able to collapse all such curves onto $\bar{\tau}_{\text{RT}}(Q)$. The assumption of Markovian behavior breaks down at short times and for unsuitable RCs (i.e., RCs that do not single out the transition state, as will be explained in detail later on) and is clearly indicated by deviations of the round-trip time functions for varying Q^f , $\tau_{\text{RT}}(Q, Q^f)$, from the mean $\bar{\tau}_{\text{RT}}(Q)$. Insight into this can be gained with a simpler definition of the diffusivity based on the variance in RC space²⁷

$$D_{\text{var}}(Q_0, \delta t) = \langle (Q(\delta t, Q_0) - \langle Q(\delta t, Q_0) \rangle)^2 \rangle / (2 \delta t), \quad (10)$$

where $Q(\delta t, Q_0)$ denotes one specific realization of a path that starts at Q_0 at time $\delta t=0$. As we will demonstrate, $D_{\text{var}}(Q_0, \delta t)$ sensitively depends on the lag time δt . To get accurate results, δt should be small enough that the region explored by the RC in this time interval has an approximately constant first derivative of the free energy; however if δt is below a threshold time scale, the resulting D_{var} may be dominated by non-Markovian properties. We will mostly use the round-trip method for determining $D(Q)$, but compare to the other methods as well.

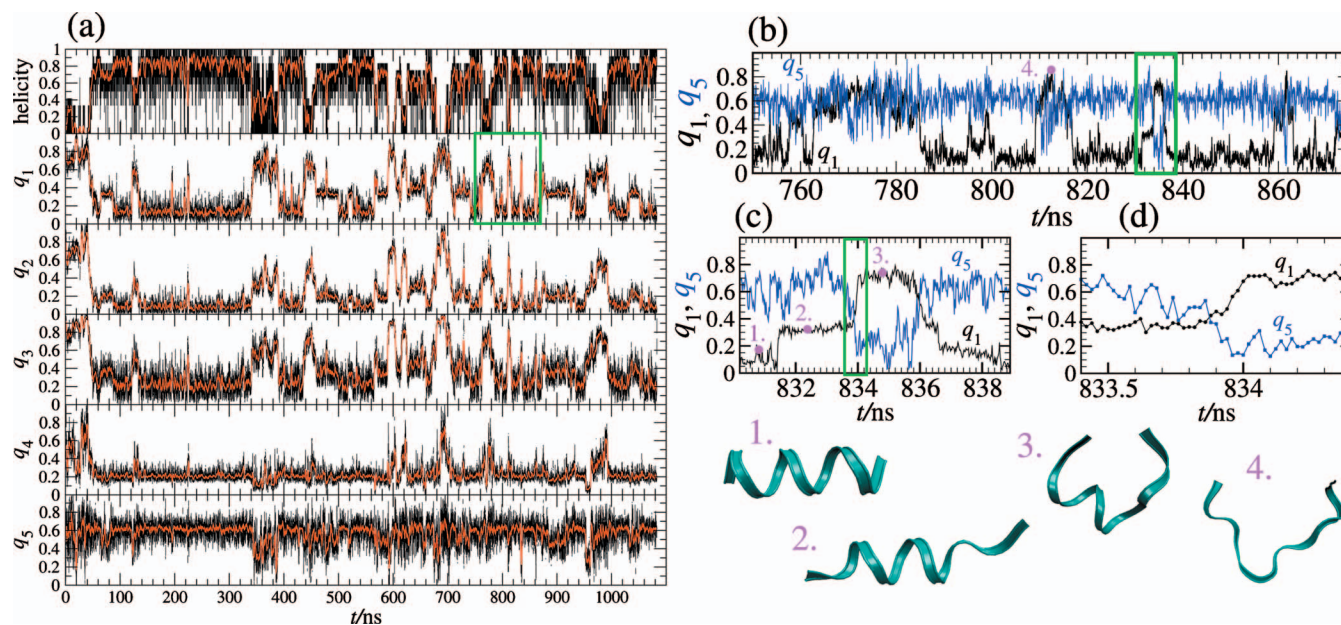


FIG. 1. Complete time series data of the simulation run for the peptide in explicit water. Shown are helicity and the five considered RCs defined in Table I. Lines in black/blue show the full resolution data (20 ps), while red lines are smoothed over time windows of 2 ns. The right panels show selected data windows at higher time resolution for q_1 and q_5 together with a few selected MD snapshots of the peptide backbone structure.

In our analysis of the simulation time series data we discretize RCs in typically $K=50$ intervals and normalize probability distributions according to $\sum_{k=1}^K \Psi(Q^{(k)}, t) = K$.

D. Fit of round-trip times

To extract $D(Q)$ from the simulation data requires estimating the derivative $\partial \bar{\tau}_{\text{RT}}(Q)/\partial Q$. We start by fitting a smooth function to the numerical results, exploiting the fact that $\bar{\tau}_{\text{RT}}(Q)$ should be a monotonically increasing function of Q . Thus the fitting function $\bar{\tau}_{\text{RT,fit}}(Q)$ can be expressed in the form

$$\bar{\tau}_{\text{RT,fit}}(Q) = \bar{\tau}_{\text{RT,fit}}(Q^{\min}) + \int_{Q^{\min}}^Q dQ' e^{W(Q')}, \quad (11)$$

where $W(Q')$ is an arbitrary function. We expand out $W(Q')$ in a basis of cubic B-splines defined over the range Q^{\min} to Q^{\max} , and use the coefficients of the expansion as fitting parameters. The size of the basis is fixed at 40 splines. The full expression for $\bar{\tau}_{\text{RT,fit}}(Q)$ is fit to the simulation estimate for $\bar{\tau}_{\text{RT}}(Q)$ using a standard least-squares technique, with one modification: the quantity to be minimized is the sum of squared residuals plus another term which penalizes roughness in the fitted function. This additional term has the form $\lambda \int_{Q^{\min}}^{Q^{\max}} dQ' (\partial W(Q')/\partial Q')^2$, with smoothing parameter λ . Larger values of λ lead to progressively smoother fits to the data. The entire fitting procedure is implemented through the Functional Data Analysis package in the R programming language.⁴⁴ For all the results shown below we set $\lambda=50$, since we found that varying λ in the range of 10–200 had minimal effect on the resulting diffusion profiles. The units of λ are $(\delta t)^2 (Q_{\max} - Q_{\min})$, where $\delta t=20$ ps is the time resolution of the MD simulation. The range $\lambda \ll 10$ is unsuitable because we fit to jagged features in the simulation $\bar{\tau}_{\text{RT}}(Q)$ curve, which are the result of statistical noise. For the range

$\lambda \gg 200$, we over-smooth the curve, losing most of the local slope information and resulting in poor fits to the round-trip function.

E. Reparameterization

As is well-known,^{45,46} the FP Eq. (2) is invariant under an arbitrary RC rescaling $\tilde{Q} = \tilde{Q}(Q)$ if the functions Ψ , F , and D are simultaneously rescaled as $\tilde{\Psi} = \Psi/\tilde{Q}'$, $\tilde{F} = F + \beta^{-1} \ln \tilde{Q}'$, and $\tilde{D} = (\tilde{Q}')^2 D$. Here, $\tilde{Q}' = d\tilde{Q}(Q)/dQ$ is assumed positive. Thus an arbitrary diffusivity profile $\tilde{D}(\tilde{Q})$ can be obtained, while the kinetics on the FP level and the partition function Z stay invariant, as long as the folding free energy is adjusted accordingly. For the particular choice of a constant diffusivity, $\tilde{D} = \tilde{D}_0$, we get $\tilde{Q}' = \sqrt{\tilde{D}_0/D}$ and thus $\tilde{F} = F - (2\beta)^{-1} \ln(D/\tilde{D}_0)$.

III. RESULTS

Figure 1 shows the complete times series data for the simulated oligopeptide. In all five RCs and in the helicity data frequent switching between the folded state (large helicity and small q_i values) and the unfolded state is observed, meaning that the simulation is converged and allows drawing conclusions on the folding and unfolding kinetics (further evidence is provided by the excellent comparison between straight MD and replica-exchange simulations, as shown in Fig. 6). The fine resolution data (Fig. 1, right panel) in terms of the rms-deviation from the fully helical state, RC q_1 , suggest that an intermediate state and two barriers are present. As the snapshots indicate, in the fully helical state ($q_1 \approx 0.1$) roughly three α -helical turns are stabilized by salt bridges between the Glu⁺-2 and Lys⁻-6 and the Glu⁺-7 and Lys⁻-11 residues, respectively. In the intermediate state ($q_1 \approx 0.4$) only one of the two salt bridges stabilizes two turns,

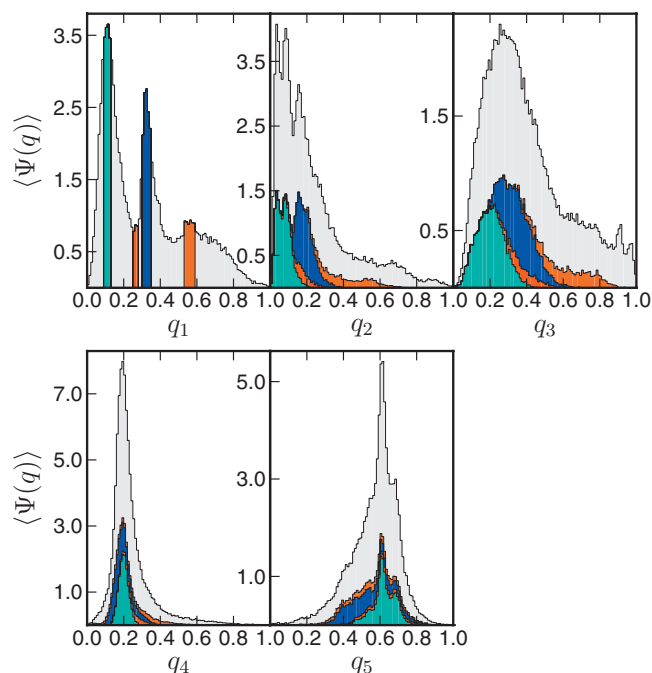


FIG. 2. Mapping from RC q_1 to different RCs. Plotted is the mean distribution $\langle \Psi(q) \rangle$ for the entire time series data in Fig. 1 and—in different colors—selected regions of the distribution corresponding to narrow intervals of q_1 values.

while in the unfolded state ($q_1 \geq 0.7$) no bridge is present. Note that the characteristic transition time for unfolding of one helical turn, i.e., for the transition from $q_1 \approx 0.4$ to $q_1 \approx 0.7$ in (d), is roughly 200 ps and thus about 100 times shorter than the corresponding unfolding time in Fig. 3(e). While a high degree of correlation between different RCs can be inferred from Fig. 1, there is no one-to-one mapping, e.g., q_5 in Fig. 1(c) shows pronounced fluctuations in intervals where q_1 stays virtually constant.

This is already evident from the average distribution function $\langle \Psi(q) \rangle$ shown in Fig. 2 as a function of all different RCs. While the distribution $\langle \Psi(q_1) \rangle$ in the leftmost panel as a function of q_1 shows three broad peaks (corresponding roughly to none, one and two intact salt bridges), clearly separated peaks are absent when $\langle \Psi \rangle$ is shown as a function of q_2, q_3, q_4 , or q_5 . The reason is simple: states that are separated when, e.g., described by q_1 , are mixed when they are projected onto different RCs. This is demonstrated by the colored regions in Fig. 2 that for q_1 correspond to pure states, i.e., narrow intervals of q_1 values. While for q_2 and q_3 , the colored regions are smeared out but the ordering along the RC is preserved, for q_4 and q_5 the ordering is lost. This points to a fundamental difference between the RCs q_1, q_2, q_3 , which embody knowledge of the native state, and the RCs q_4, q_5 , which are purely geometric.

In Fig. 3, we focus on RC q_1 . The free-energy profile $\beta F(q_1) = -\ln \langle \Psi(q_1) \rangle$ in a) reveals the intermediate state and two barriers at $q_1 \approx 0.26$ and $q_1 \approx 0.48$. Figure 3(b) shows the roundtrip times $\tau_{RT}(q_1, q_1^f)$ for various final states q_1^f as a function of q_1 , directly extracted from the simulation time series.⁴⁷ The data sets are shifted vertically [which according to Eq. (9) is irrelevant for extracting $D(q_1)$] to illustrate the

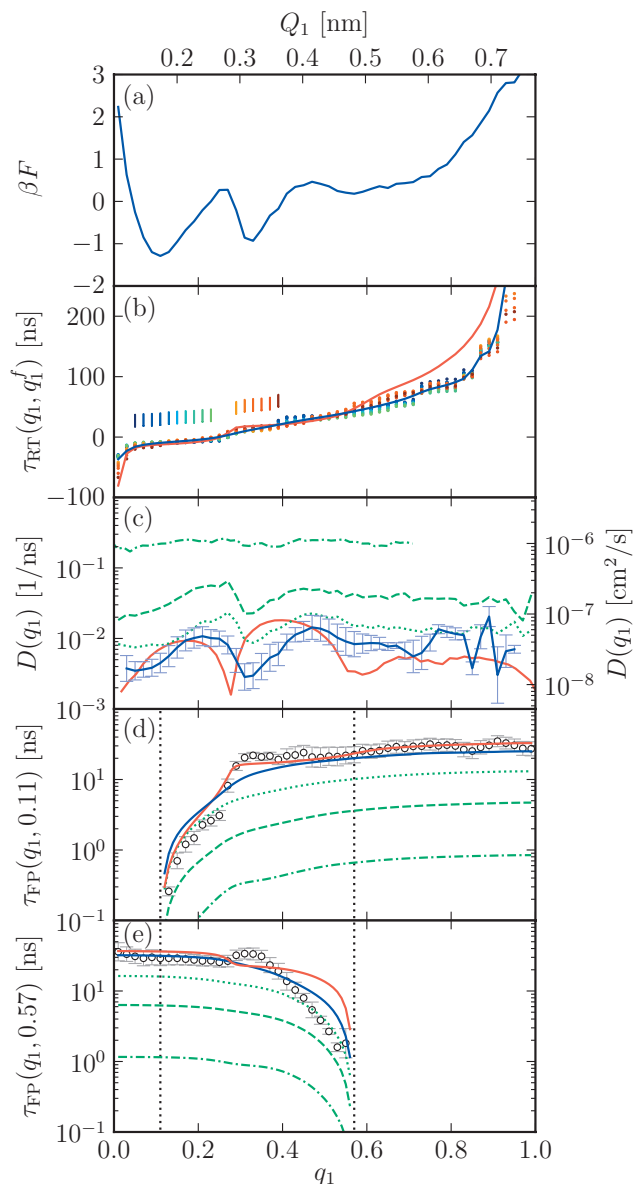


FIG. 3. Results for RC q_1 (note that the upper scale is in terms of the unrescaled RC Q_1). (a) Free-energy profile $\beta F = -\ln \langle \Psi \rangle$. (b) Data points give the round-trip times $\tau_{RT}(q_1, q_1^f)$ as extracted from the simulation data for various final states q_1^f that are denoted by vertical colored bars. The data is shifted vertically for each q_1^f to illustrate the theoretically predicted collapse onto a single mean round-trip time function $\bar{\tau}_{RT}(q_1)$, with the smooth fit $\bar{\tau}_{RT,fit}(q_1)$ shown in blue. The red curve denotes the round-trip time from the Bayesian approach. (c) Diffusivity from the round-trip time method equation (9) (blue curve), compared to the variance method equation (10) for lag times $\delta t = 200$ fs, 20 ps, and 200 ps (dash-dotted, dashed, and dotted green curves), and to the Bayesian method (red curve) (Ref. 42). (d) MFP or folding time $\tau_{FP}(q_1, q_1^f)$ for the final state $q_1^f = 0.11$, as extracted directly from the simulation data (circles) and compared to predictions from Eq. (3) using the different diffusivities shown in (c). (e) MFP or unfolding time for the final state $q_1^f = 0.57$, same notation as in (d). Vertical dotted lines in [(d) and (e)] mark the final states q_1^f for folding and unfolding.

predicted collapse onto a single mean round-trip time function $\bar{\tau}_{RT}(q_1)$. The smooth fit $\bar{\tau}_{RT,fit}(q_1)$ is shown as a blue curve. The collapse of $\tau_{RT}(q_1, q_1^f)$ for different q_1^f is a strong check on the consistency of the FP approach. The red curve denotes the round-trip time from the Bayesian approach,⁴² obtained for optimized time interval and smoothing parameters $\Delta t = 6$ ns and $\gamma = 0.2$ ns⁻¹.⁴⁷ Figure 3(c) shows the dif-

fusivity $D(q_1)$ extracted from $\bar{\tau}_{\text{RT,fit}}(q_1)$ via Eq. (9) (blue curve). Most notably, $D(q_1)$ varies considerably along q_1 : it is reduced by an order of magnitude around the intermediate state at $q_1 \approx 0.32$ and seems correlated with $F(q_1)$. The $D(q_1)$ profile from the Bayesian approach (red curve) reproduces the coarse features of our round-trip approach with a slight difference that will be discussed below. We stress that we have fitted the two parameters in the Bayesian approach, namely, the time interval and the smoothing parameter, by a comparison with the simulation mean-first passage times (see supplement for further details⁴⁷). The diffusivity profiles resulting from the Bayesian approach sensitively depend on these parameters, and without such a comparison, it is not easy to see what are the sensible parameter values. This highlights an advantage of our method based on the round-trip time, since the only parameter is a smoothing factor that operates directly on the round-trip time, a physical observable, and sensible parameter values are straightforwardly estimated. The variance method equation (10) for lag time $\delta t = 200$ fs (upper green curve) overestimates $D(q_1)$ by two orders of magnitude, yet for $\delta t = 200$ ps (lower green curve) D_{var} approaches the results of the other two methods quite nicely. Thus for $\delta t < 200$ ps, D_{var} is dominated by non-Markovian events that are unrelated to the long-time folding/unfolding dynamics; interestingly, this threshold time is similar to the transition time for helix unwrapping inferred from Fig. 1(d). In Figs. 3(d) and 3(e), we show MFP times $\tau_{\text{FP}}(q_1, q_1^f)$ for $q_1 > q_1^f = 0.11$ (folding) and $q_1 < q_1^f = 0.57$ (unfolding) calculated from Eq. (3) and the various $D(q_1)$ profiles shown in (c). $\tau_{\text{FP}}(q_1, q_1^f)$ directly extracted from simulation data (circles) in Fig. 3(d) is most accurately reproduced by the Bayesian fitting approach (red curve), as expected since the probability distribution and thus the frequency of transitions is maximal in the range $q_1 \approx 0-0.25$ [see Fig. 2(a)]. The RT approach (blue curve) considers an equal balance of folding and unfolding events and consequently describes unfolding MFP times in Fig. 3(e) better. Notably, the RT approach is simple to implement, directly works on the property one wishes to describe (namely, folding/unfolding times) and has apart from the functional form of the fitted round-trip time $\bar{\tau}_{\text{RT}}(q_1)$ no freely adjustable parameter. The combined deviations between simulation data and FP predictions in Figs. 3(d) and 3(e) are due to a combination of non-Markovian processes at short times and insufficient trajectory sampling.

In Fig. 4(a), we compare the diffusivities based on the round-trip time approach (blue curve) and the Bayesian approach (red curve), already presented in Fig. 3(c), with results obtained from the MFP times via Eq. (5), shown as a green curve. For the fit we used a final state $q_1^f = 0.11$ and considered folding events from $q_1 > q_1^f$ to q_1^f . It is seen that the three curves roughly coincide, which testifies to the robustness of methods for deriving diffusivities from folding times. In Fig. 4(b), we compare diffusivities from the variance method, Eq. (10), to the round-trip time method Eq. (9) (blue curve). Here we present results for $D_{\text{var}}(Q, \delta t)$ for a wider range of lag times of $\delta t = 200$ fs, 20 ps, 200 ps, 2 ns, and 10 ns (green curves, from top to bottom). It is seen that for lag times between $\delta t = 200$ ps and $\delta t = 2$ ns, $D_{\text{var}}(Q, \delta t)$

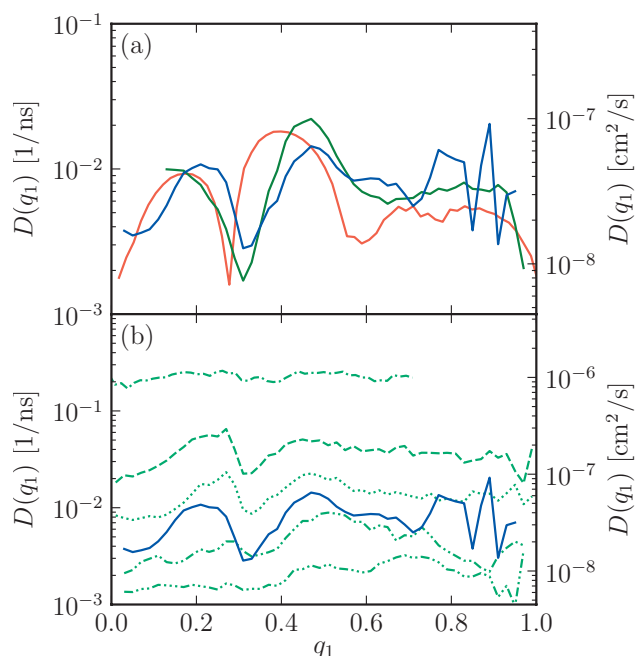


FIG. 4. Results for RC q_1 . (a) Diffusivity from round-trip time method Eq. (9) (blue curve) and the Bayesian approach (red curve); these are the same data already shown in Fig. 3(c). The green curve is based on the first passage time method and follows from Eq. (5) for the final state $q_1^f = 0.11$. (b) Diffusivity from the round-trip time method Eq. (9) (blue curve) compared to the variance method Eq. (10) for lag times $\delta t = 200$ fs, 20 ps, 200 ps, 2 ns, and 10 ns (green curves, from top to bottom).

agrees with the round-trip time approach. As already discussed, for smaller lag times $D_{\text{var}}(Q, \delta t)$ is too large. For larger lag times $D_{\text{var}}(Q, \delta t)$ loses structure and becomes too small, which has to do with the fact that at those times the peptide explores a considerable subsection of the free-energy space and the effect of the energetic barriers encountered is spuriously accounted for by a reduction of the diffusivity. The situation is similar to the Bayesian approach: there is no a-priori way of knowing what the suitable parameter value for the lag time is, unless one compares to a physical observable, which might be the folding or round-trip time. In that case, however, a direct fitting of $D(q)$ based on folding times as suggested by us seems more direct and transparent.

A free-energy barrier, as exhibited by $F(q_1)$ in Fig. 3(a), was argued to arise from a subtle compensation of energy and entropy effects, which both increase upon unfolding.³ This scenario, developed in the context of lattice models, is basically confirmed by our explicit water simulations. In Fig. 5(a), we show free-energy profiles at different temperatures T from replica-exchange simulations. Indeed, the entropic contribution TS , estimated from the free-energy difference between $T = 280$ and 320 K, shows considerable numerical error but rises across the unfolding transition. In Fig. 5(b), we show the number N_{wat} of backbone-bound water molecules that have a distance to a backbone oxygen smaller than 0.35 nm. Apart from the loss of one bound water molecule at $q_1 \approx 0.3$ (paralleled by a helicity increase), N_{wat} steadily rises from about $N = 20$ in the folded state to $N = 30$ in the unfolded state. So we conclude that the entropy increase upon unfolding results from a competition of water binding and conformational effects. The overall good com-

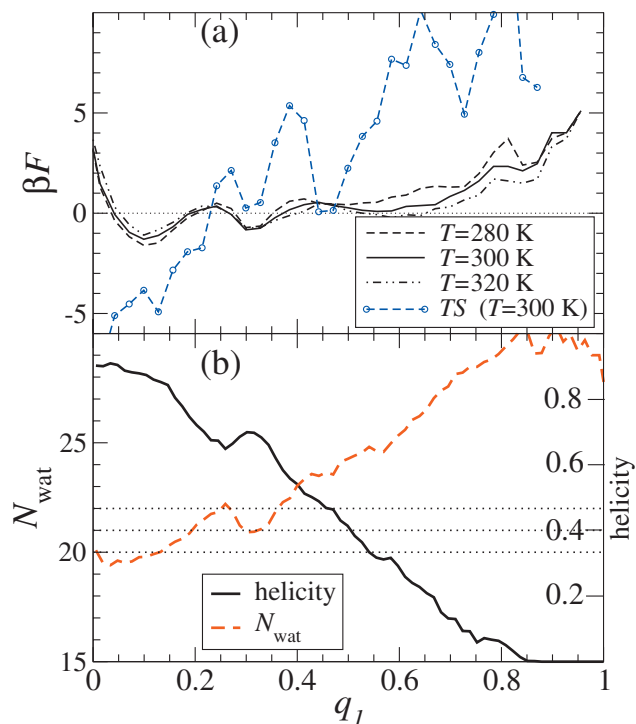


FIG. 5. (a) REMD results for the free-energy profile $\beta F(q_1)$ for different temperatures T , together with the entropic contribution TS obtained from the finite- T difference (with $\Delta T=20$ K) of $\beta F(q_1)$. (b) Helicity and the number N_{wat} of backbone-bound water molecules vs. q_1 at $T=300$ K. The horizontal broken lines denote 20, 21, and 22 backbone-bound water molecules.

parison between the free-energy profile from a standard MD simulation run (for a length of $1.1 \mu\text{s}$) and results from a replica exchange MD simulation (trajectory length 22.5 ns and equilibrated with 32 replicas at different temperatures) at $T=300$ K in Fig. 6 gives good evidence that the times series considered in our kinetic analysis is long enough.

The appearance of a free-energy barrier, as seen in $F(q_1)$ in Fig. 3(a), is often interpreted as equivalent to exponential kinetics, which is not necessarily true as we will now discuss. In fact, even the presence of a free-energy barrier depends on the specific RC employed and thus is a much less robust feature than often assumed. In Fig. 7, we show the

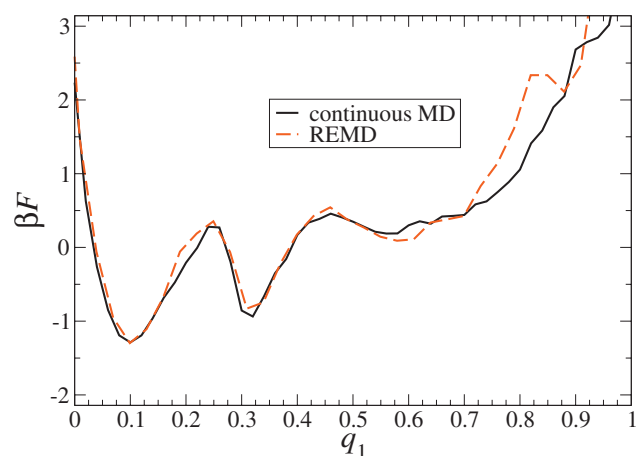


FIG. 6. Comparison between REMD results (red broken curve) and standard MD results (black solid curve) for the free-energy profile $\beta F(q_1)$ at $T=300$ K.

free energy $F(q_i)$ and diffusivity $D(q_i)$ profiles of all five RCs. We separate RCs that embody knowledge of the native state q_1, q_2, q_3 and the unbiased RCs q_4, q_5 . In the columns marked “original,” we use the bare RCs q_i as defined in Sec. II; in the columns marked “transformed,” we use rescaled RCs \tilde{q}_i such that the diffusivities are constant, $\tilde{D}(\tilde{q}_i)=\tilde{D}_0$. Two features strike the eyes:

- (i) Most diffusivity profiles are full of structure and vary substantially along the reaction path; it immediately transpires that a description of the folding kinetics without consideration of the diffusivity profile can fail.
- (ii) The profiles $F(q_i)$ and $D(q_i)$ vary considerably among different RCs. In fact, while $F(q_1)$ shows pronounced barriers and an intermediate state, the profiles $F(q_2)$ and $F(q_3)$ are free of barriers: We conclude that the presence of barriers depends on the RC chosen.

Do the kinetics within an effective FP description also vary among RCs, possibly showing exponential for some and nonexponential behavior for other RCs? While the free-energy profiles $F(q_i)$ as a function of the original RCs show large variations, the profiles $\tilde{F}(\tilde{q}_i)$ after the transformation are quite similar (this is most striking for the radius of gyration, \tilde{q}_4 , and the end-to-end radius, \tilde{q}_5), and thus the kinetics as characterized by the MFP times $\tau_{\text{FP}}(q_i, q_i^f)$ in the bottom row are very similar. This at first surprising result can be easily rationalized: the round-trip method is designed to optimally reproduce the complete set of round-trip times and thus the slowest conformational transitions in the system. The different diffusivities $D(q_i)$ and free-energy profiles $F(q_i)$ together uniquely determine the folding times. Assuming that different RCs yield a comparable separation of states into the unfolded and folded basins, it follows that the folding times must be very similar. This in fact holds for the RCs q_1, q_2, q_3 on the one hand and for the RCs q_4, q_5 on the other hand. Since after the rescaling the entire kinetic information is contained in the free-energy profile, those profiles must be quite similar. It follows that the presence of a free-energy barrier does not necessarily imply exponential kinetics; for that statement to be true the free-energy barrier must persist after a RC transformation that makes the diffusivity profile flat. Although there are still differences among the free-energy profiles for q_1, q_2, q_3 after the transformation, they are small enough that the kinetics are not particularly distinguished.

To highlight the implications of these results, we now turn the argumentation around. Consider a general RC transformation

$$\tilde{q} = q + c(\tanh[(q - q^*)/d] - 1), \quad (12)$$

which is assumed to be a monotonic function implying that $d > -c$. This rescaling corresponds to a local stretching/compression of the RC around q^* and via the reparametrization properties of the FP equation also modifies the diffusivity and the free-energy profiles. In Fig. 8, we show three different rescaled $\tilde{F}(\tilde{q}_1)$ and $\tilde{D}(\tilde{q}_1)$ profiles, all generated via Eq. (12) from the RC \tilde{q}_1 for which $\tilde{D}(\tilde{q}_1)$ is flat (shown in

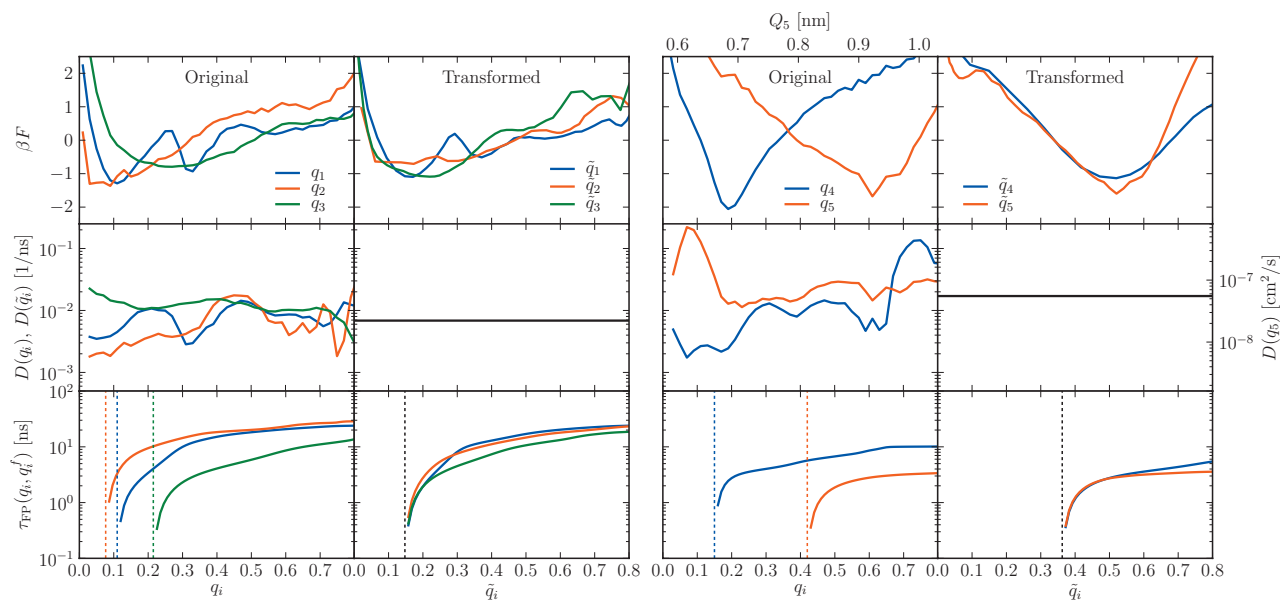


FIG. 7. Free-energy profiles (top row), diffusivity profiles (middle row), and folding MFP times (bottom row) for all five RCs. The columns denoted original show results as a function of the original RCs q_i , while in the columns denoted transformed, rescaled coordinates \tilde{q}_i are used such that the diffusivity profiles are constant. The final states q_i^f for the folding (marked by dotted vertical lines) are chosen such that they map onto a single value \tilde{q}_i^f separately for the q_1, q_2, q_3 and q_4, q_5 groups.

blue). Depending on the parameters q^*, c, d we generate free-energy profiles that either exhibit a more pronounced barrier (green curve), a reduced barrier (red curve), or a free-energy profile where the position of the minimum is moved from the folded to the unfolded state (turquoise curve). We mention that by construction, the kinetics as characterized by the

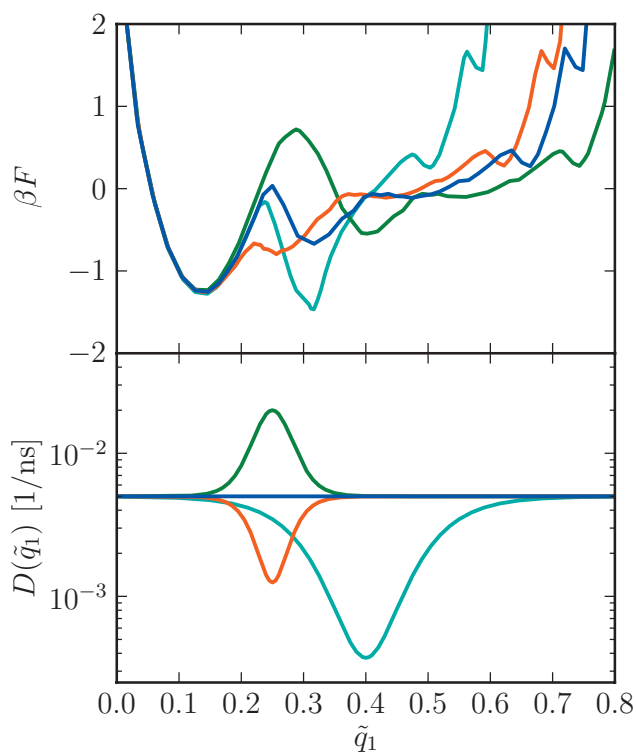


FIG. 8. Free-energy (top) and diffusivity profiles (bottom) for different rescaled RCs \tilde{q}_1 . Starting from the RC exhibiting a flat diffusivity (shown in blue), we arbitrarily rescale \tilde{q}_1 according to Eq. (12) such as to increase the barrier (green), decrease the barrier (red) and to relocate the stable minimum (turquoise).

round trip or MFP time is invariant under this rescaling. What this figure demonstrates is that under a combined rescaling of $F(q)$ and $D(q)$ one can generate a bewildering variety of free-energy curves which share the identical kinetics, meaning that the free-energy profile without the diffusivity is not sufficient to even qualitatively predict protein folding kinetics.

Much of the preceding discussion and the usage of one-dimensional RCs presumes that the RCs are “good” in the sense that (i) the ensemble of transition states is assigned to a narrow region of RC values and (ii) that the probability of finding a transition state in that region is maximal.^{33,34} To make that notion more concrete, one introduces the splitting probabilities $\phi^A(q)$ and $\phi^B(q)$ for each value of the RC, where $\phi^A(q)$ is the probability to reach, starting from RC value q , region A before region B.³⁴ In the context of transition states, the regions A and B would denote regions corresponding to the folded and unfolded domains flanking the transition region. The splitting probabilities are normalized as

$$\phi^A(q) + \phi^B(q) = 1, \quad (13)$$

since eventually any state will diffuse out toward the boundaries. For a trajectory that passes through state q_1 , there are four choices: it can be trajectory starting in A and returning to A, starting in B and returning B, starting in A and ending up in B or starting in B and ending in A. The respective probabilities are normalized as

$$P(A \rightarrow A|q) + P(A \rightarrow B|q) + P(B \rightarrow A|q) + P(B \rightarrow B|q) = 1. \quad (14)$$

For nonballistic stochastic motion, the transition path probability $P(\text{TP}|q) = P(A \rightarrow B|q) + P(B \rightarrow A|q)$, i.e., the probability that the trajectory connects regions A and B, can be maximally 1/2. A maximum close to 1/2 characterizes a good

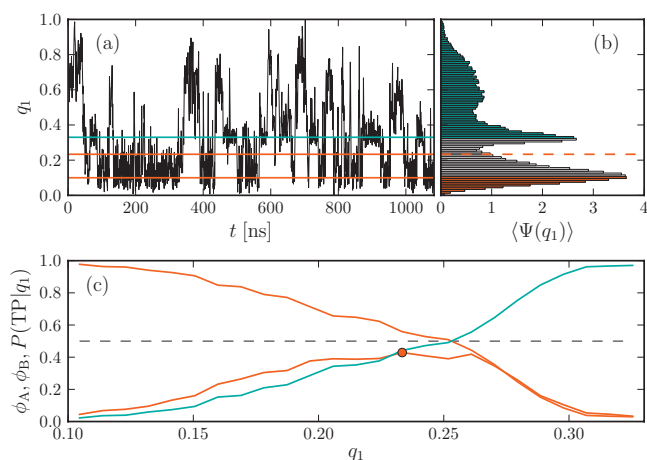


FIG. 9. Test for the quality of RC q_1 . (a) shows the complete trajectory, (b) shows the corresponding equilibrium distribution $\langle \psi(q_1) \rangle$ and the regions A ($q_1 < 0.1$) and B ($q_1 > 0.33$) marked in orange and blue, respectively. The complete trajectory contains 181 transitions between A and B (90 from A to B and 91 from B to A). Panel (c) shows the splitting probabilities $\phi^A(q_1)$ (orange) and $\phi^B(q_1)$ (blue) and the transition path probability $P(\text{TP}|q_1)$ (red). $P(\text{TP}|q_1)$ reaches the maximum value $P(\text{TP}|q_1) \approx 0.43$ for $q_1 = q_1^\ddagger \approx 0.23$, denoted by a red circle in (c) and red lines in [(a) and (b)].

RC, a significantly smaller number points to a bad RC. In Fig. 9, we show a detailed RC analysis for RC q_1 with a resolution of 25 bins in the range $0.1 < q_1 < 0.33$ and using the full time resolution of 20 ps. In (a), we show again the complete time series and in (b) the corresponding probability distribution. Region A for $q_1 < 0.1$ is the folded region; region B for $q_1 > 0.33$ is a region where one helical turn is unfolded. In (c), we show the splitting probabilities $\phi^A(q_1)$ and $\phi^B(q_1)$ (orange and blue lines). The behavior is as expected, with the probabilities switching from zero to unity between the boundaries of the regions A and B, and a rather large slope in the region around $q_1 \approx 0.25-0.30$. The maximum of the transition path probability $P(\text{TP}|q_1^\ddagger) \approx 0.43$ (shown as a red curve) at a position $q_1^\ddagger \approx 0.23$ means that q_1 is quite close to a perfect RC and that the FP analysis performed in this paper is appropriate for long times on the order of folding and unfolding events. Note that $q_1^\ddagger \approx 0.23$ is close to a minimum in the equilibrium distribution $\langle \psi(q_1) \rangle$, see Fig. 9(b), at which position the free energy thus exhibits a maximum. This is coincidental, since as we have shown in Fig. 8, one can easily change the free-energy profile by a reaction-coordinate rescaling, which however leaves the splitting probabilities and the transition path probabilities invariant.

IV. CONCLUSIONS

In the naive approach toward protein kinetics, folding times are deduced from the free-energy profile $F(Q)$ alone. As has been argued before,²⁴⁻²⁷ such an approach is unreliable since for the simplest nontrivial folder, namely, a single short α -helix in explicit solvent, the diffusivity profile $D(Q)$ varies substantially along the folding path. Our $D(Q)$ variation comes out somewhat stronger than from similar simulations with implicit solvent, suggesting that explicit solvent further increases the importance of diffusivity inhomogeneities.²⁴ In fact, to match experimental folding

times of simple α -helix-forming oligopeptides within solvent-implicit simulations, an overall correction factor to the time scales is typically applied.^{48,49} A detailed microscopic justification for this is lacking; on the contrary, it has been shown that in many cases explicit solvent strongly influences the free-energy landscape and introduces novel kinetic mechanisms that are completely absent in solvent-implicit simulations.^{50,51} When extending the analysis to five different popular RCs, we find free-energy and diffusivity profiles to vary substantially among different RC representations. Yet, the kinetics that follows from an FP description is largely independent of the RC chosen, if and only if $D(Q)$ is properly accounted for. A similar conclusion was reached recently based on coarse-grained, solvent-implicit simulations.²⁶ This means that a quasi-universal (i.e., RC independent) description of protein folding kinetics necessarily involves $D(Q)$. For this quasi-universality to hold we have to distinguish between RCs that are based on the distance to the native state (such as Q_1, Q_2, Q_3) and those that are purely geometric in nature (such as Q_4, Q_5). By considering generalized RCs and using the reparametrization invariance of the FP equation, we can design arbitrary $F(Q)$ profiles with no barrier at all, an enhanced barrier, or an interchange of the naive stable and unstable states. This means that the concept of a free-energy profile is to some degree arbitrary, which might be relevant with regards to recent discussions in the experimental literature.¹¹⁻¹³ The kinetics, embodied in the folding time, and dependent on $F(Q)$ and $D(Q)$, is less arbitrary.

Our simulations are for a single α -helix fragment, one of the shortest oligopeptides which shows nontrivial folding. There is no reason to believe that for larger proteins the situation will simplify; we therefore argue that the diffusivity profile will be full of features and thus important in those more complicated situations as well. Our conclusions also apply to optimized or otherwise carefully selected RCs,³³⁻³⁷ since the reparametrization can be done for any RC and thus arbitrarily create, annihilate and shift barriers in the folding landscape (incidentally, RC q_1 turns out to be a quite good RC according to the definition of Ref. 34, as shown in Fig. 9). Our method of extracting the diffusivity profile via the mean-first-passage or round-trip time formalism can be easily applied to time series data from FRET or force-spectroscopic experiments, so an experimental test of our results is possible.

ACKNOWLEDGMENTS

We acknowledge support from the Deutsche Forschungsgemeinschaft (DFG) within the contract SFB 863 and the Emmy-Noether-Programme (J.D.). The Leibniz Rechenzentrum (LRZ) Munich is acknowledged for supercomputing access.

¹E. Shakhnovich, *Chem. Rev. (Washington, D.C.)* **106**, 1559 (2006).

²K. A. Dill, S. B. Ozkan, M. S. Shell, and T. R. Weikl, *Annu. Rev. Biophys.* **37**, 289 (2008).

³M. Oliveberg and P. G. Wolynes, *Q. Rev. Biophys.* **38**, 245 (2005).

⁴A. Fersht, *Structure and Mechanism in Protein Science* (W.H. Freeman and Company, New York, 1999).

⁵T. Cellmer, E. R. Henry, J. Hofrichter, and W. A. Eaton, *Proc. Natl. Acad.*

- Sci. U.S.A.* **105**, 18320 (2008).
- ⁶ A. Möglich, K. Joder, and T. Kiefhaber, *Proc. Natl. Acad. Sci. U.S.A.* **103**, 12394 (2006).
- ⁷ B. Fierz, A. Reiner, and T. Kiefhaber, *Proc. Natl. Acad. Sci. U.S.A.* **106**, 1057 (2009).
- ⁸ E. Rhoades, M. Cohen, B. Schuler, and G. Haran, *J. Am. Chem. Soc.* **126**, 14686 (2004).
- ⁹ H. S. Chung, M. Louis, and W. A. Eaton, *Proc. Natl. Acad. Sci. U.S.A.* **106**, 11837 (2009).
- ¹⁰ H. Dietz and M. Rief, *Proc. Natl. Acad. Sci. U.S.A.* **103**, 1244 (2006).
- ¹¹ H. Ma and M. Gruebele, *Proc. Natl. Acad. Sci. U.S.A.* **102**, 2283 (2005).
- ¹² P. Li, F. Y. Oliva, A. N. Naganathan, and V. Munoz, *Proc. Natl. Acad. Sci. U.S.A.* **106**, 103 (2009).
- ¹³ F. Huang, L. Ying, and A. R. Fersht, *Proc. Natl. Acad. Sci. U.S.A.* **106**, 16239 (2009).
- ¹⁴ C. J. Camacho and D. Thirumalai, *Proc. Natl. Acad. Sci. U.S.A.* **90**, 6369 (1993).
- ¹⁵ D. Thirumalai, *J. Phys. I* **5**, 1457 (1995).
- ¹⁶ K. W. Plaxco, K. T. Simons, and D. Baker, *J. Mol. Biol.* **277**, 985 (1998).
- ¹⁷ N. Agmon and J. J. Hopfield, *J. Chem. Phys.* **79**, 2042 (1983).
- ¹⁸ N. D. Socci, J. N. Onuchic, and P. G. Wolynes, *J. Chem. Phys.* **104**, 5860 (1996).
- ¹⁹ R. Du, V. S. Pande, A. Y. Grosberg, T. Tanaka, and E. S. Shakhnovich, *J. Chem. Phys.* **108**, 334 (1998).
- ²⁰ R. Zwanzig, *Proc. Natl. Acad. Sci. U.S.A.* **85**, 2029 (1988).
- ²¹ R. Zwanzig, *J. Chem. Phys.* **97**, 3587 (1992).
- ²² N. A. Denesyuk and J. D. Weeks, *Phys. Rev. Lett.* **102**, 108101 (2009).
- ²³ A. Alexander-Katz, H. Wada, and R. R. Netz, *Phys. Rev. Lett.* **103**, 028102 (2009).
- ²⁴ R. B. Best and G. Hummer, *Phys. Rev. Lett.* **96**, 228104 (2006).
- ²⁵ J. Chahine, R. J. Oliveira, V. B. P. Leite, and J. Wang, *Proc. Natl. Acad. Sci. U.S.A.* **104**, 14646 (2007).
- ²⁶ R. B. Best and G. Hummer, *Proc. Natl. Acad. Sci. U.S.A.* **107**, 1088 (2010).
- ²⁷ S. Yang, J. N. Onuchic, A. E. Garcia, and H. Levine, *J. Mol. Biol.* **372**, 756 (2007).
- ²⁸ S. Marqusee and R. L. Baldwin, *Proc. Natl. Acad. Sci. U.S.A.* **84**, 8898 (1987).
- ²⁹ J. Dzubiella, *J. Am. Chem. Soc.* **130**, 14000 (2008).
- ³⁰ M. T. Woodside, P. C. Anthony, W. M. Behnke-Parks, K. Larizadeh, D. Herschlag, and S. M. Block, *Science* **314**, 1001 (2006).
- ³¹ J. C. M. Gebhardt, T. Bornschlögl, and M. Rief, *Proc. Natl. Acad. Sci. U.S.A.* **107**, 2013 (2010).
- ³² C. Hyeon and D. Thirumalai, *J. Am. Chem. Soc.* **130**, 1538 (2008).
- ³³ P. G. Bolhuis, D. Chandler, C. Dellago, and P. L. Geissler, *Annu. Rev. Phys. Chem.* **53**, 291 (2002).
- ³⁴ R. B. Best and G. Hummer, *Proc. Natl. Acad. Sci. U.S.A.* **102**, 6732 (2005).
- ³⁵ L. Maragliano, A. Fischer, E. Vanden-Eijnden, and G. Ciccotti, *J. Chem. Phys.* **125**, 024106 (2006).
- ³⁶ M. Sega, P. Faccioli, F. Pederiva, G. Garberoglio, and H. Orland, *Phys. Rev. Lett.* **99**, 118102 (2007).
- ³⁷ F. Noe, C. Schütte, E. Vanden-Eijnden, L. Reich, and T. R. Weikl, *Proc. Natl. Acad. Sci. U.S.A.* **106**, 19011 (2009).
- ³⁸ T. Ghosh, S. Garde, and A. E. Garcia, *Biophys. J.* **85**, 3187 (2003).
- ³⁹ D. A. Case, AMBER 9.0 software, University of California, San Francisco (2006).
- ⁴⁰ W. Kabsch and D. Sander, *Biopolymers* **22**, 2577 (1983).
- ⁴¹ P. Hänggi, P. Talkner, and M. Borkovec, *Rev. Mod. Phys.* **62**, 251 (1990).
- ⁴² G. Hummer, *New J. Phys.* **7**, 34 (2005).
- ⁴³ G. H. Weiss, *Adv. Chem. Phys.* **13**, 1 (1966).
- ⁴⁴ J. O. Ramsay, G. Hooker, and S. Graves, *Functional Data Analysis with R and MATLAB* (Springer, New York, 2009).
- ⁴⁵ Y. M. Rhee and V. S. Pande, *J. Phys. Chem. B* **109**, 6780 (2005).
- ⁴⁶ S. V. Krivov and M. Karplus, *Proc. Natl. Acad. Sci. U.S.A.* **105**, 13841 (2008).
- ⁴⁷ See supplementary material at <http://dx.doi.org/10.1063/1.3442716> for full details of the mapping between RCs and extracting the diffusivity profile through first-passage/Bayesian methods.
- ⁴⁸ S. Chowdhury, W. Zhang, C. Wu, G. Xiong, and Y. Duan, *Biopolymers* **68**, 63 (2003).
- ⁴⁹ W.-Z. Wang, T. Lin, and Y.-C. Sun, *J. Phys. Chem. B* **111**, 3508 (2007).
- ⁵⁰ R. Zhou, *Proteins* **53**, 148 (2003).
- ⁵¹ Y. M. Rhee, E. J. Sorin, G. Jayachandran, E. Lindahl, and V. S. Pande, *Proc. Natl. Acad. Sci. U.S.A.* **101**, 6456 (2004).